

## Scaling theory of drying in porous media

I. N. Tsimpanogiannis and Y. C. Yortsos\*

*Department of Chemical Engineering, University of Southern California, Los Angeles, California 90089-1211*

S. Poulou, N. Kanellopoulos, and A. K. Stubos

*National Center for Scientific Research "Demokritos," 15310 Aghia Paraskevi, Greece*

(Received 2 November 1998)

Concepts of immiscible displacements in porous media driven by mass transfer are utilized to model drying of porous media. Visualization experiments of drying in two-dimensional glass micromodels are conducted to identify pore-scale mechanisms. Then, a pore network approach is used to analyze the advancing drying front. It is shown that in a porous medium, capillarity induces a flow that effectively limits the extent of the front, which would otherwise be of the percolation type, to a finite width. In conjunction with the predictions of a macroscale stable front, obtained from a linear stability analysis, the process is shown to be equivalent to invasion percolation in a stabilizing gradient. A power-law scaling relation of the front width with a diffusion-based capillary number is also obtained. This capillary number reflects the fact that drying is controlled by diffusion in contrast to external drainage. The scaling exponent predicted is compatible with the experimental results of Shaw [Phys. Rev. Lett. **59**, 1671 (1987)]. A framework for a continuum description of the upstream drying regimes is also developed. [S1063-651X(99)04604-8]

PACS number(s): 81.05.Rm

### I. INTRODUCTION

The drying of porous media is a problem of significant scientific and applied interest. Chen and Pei [1] note that drying is one of the most energy-consuming processes in industry. Applications include the drying of granular materials such as soils, rocks, minerals, building materials, and ceramic powders; drying processes in the wood (Simpson [2,3]), paper, and textile industry; coating technology; and the drying of foodstuff (Fortes and Okos [4]) and pharmaceutical products. In a different context, *in situ* drying of porous media is involved in recent methods for the remediation of contaminated soils by soil vapor extraction or soil venting (Ho and Udell [5]), as well as in the recovery of volatile hydrocarbons from underground oil reservoirs by gas injection (Le Romancer *et al.* [6], Le Gallo *et al.* [7]).

The development of a general mathematical framework to model drying of porous media has been a rather challenging research topic for several decades (Waananen *et al.* [8]). Although a plethora of methods have been presented, and while industrial designers are faced with the demand to design complicated processes regarding "real" problems, there are still many unresolved questions, even for "simpler" problems (Prat [9]). Traditionally, the description of drying in porous media is based on phenomenological approaches that consider the medium as a structureless continuum. In these, partial differential equations are postulated that relate the evolution in spacetime of volume-averaged quantities, such as moisture content and temperature. Phenomenological and empirical parameters are then used to relate fluxes to gradients, often drawn from an analogy with nonequilibrium thermodynamics (for example, see Luikov [10]). However, in these approaches, the pore microstructure and the underlying

phenomena, which are key to the quantitative understanding of the process, are essentially ignored.

On a fundamental level, drying is a phase change of a (usually) one-component liquid into a (usually) two-component gas, and involves at various stages the motion (receding) of individual gas-liquid menisci (see schematic of Fig. 1). The menisci reside in the pore space of the porous medium and are subject to the interfacial forces between liquid, gas, and solid surfaces. Due to the disorder in the pore space geometry, however, their distribution is also disordered in general. The physical processes involve evaporation of the volatile liquid in the gas phase, driven by concentration gradients, countercurrent diffusion in the gas, possible liquid flow through connected films, and the accompanying receding of menisci. All these interactions are influenced by the porous medium microstructure to a significant degree.

In general, four different spatial regimes can be distinguished during a drying process (Fig. 2): A far-field regime consisting of the initial liquid phase, a regime where the liquid phase is macroscopically connected and where both

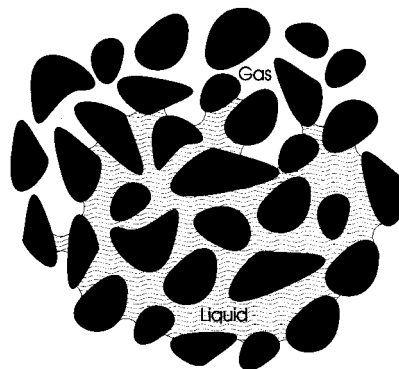


FIG. 1. Schematic of liquid-gas interfaces during drying in porous media.

\*Author to whom correspondence should be addressed.

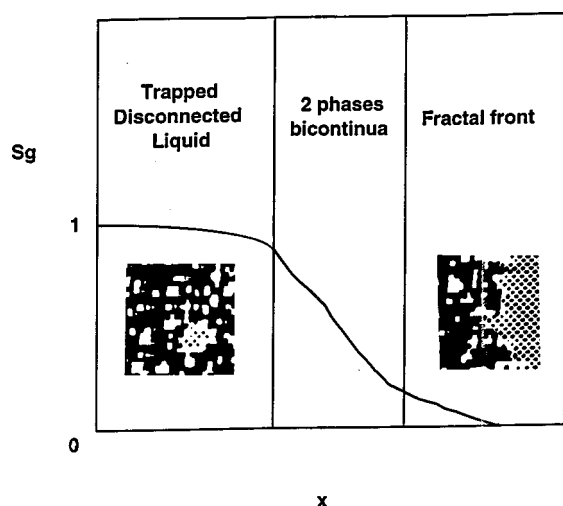


FIG. 2. Schematic description of drying regimes in porous media, obtained from 2D pore network simulations. Dots and white areas denote liquid-occupied regions, dark shaded areas denote gas-occupied regions. (Due to the 2D topological limitations, a schematic of the 2-phase bicontinuum regime is not feasible.)

gas and liquid phases are “macroscopically continuous,” a third regime in which the liquid phase has been disconnected in individual clusters of variable sizes (blobs) as a result of drying, and a fourth regime consisting of the liquid phase in the form of pendular rings or films covering the solid surface, the thickness of which is progressively reduced, towards a “totally dry” regime. In the last three regimes the gas phase is macroscopically continuous. Shaw [11] has also postulated that liquid films may provide hydraulic connectivity to the liquid phase in all three regimes. It is apparent that an appropriate account of the various pore-scale events in all these regimes is fundamental to the accurate representation of any macroscopic description (Whitaker [12]).

Pore-network approaches for describing drying of porous media were recently proposed by Nowicki, Davis, and Scriven [13] and in a series of papers by Prat and co-workers (Prat [14,15], Laurindo and Prat [16,17]). In a related context, Pot *et al.* [18] used lattice-gas cellular automata to simulate evaporation phenomena in two-dimensional (2D) porous media. Nowicki, Davis, and Scriven [13] developed a rather comprehensive pore-network simulation of the process, and accounted for both capillary and viscous forces. However, the authors did not delve into the particular patterns that develop or on their effect on the drying rates. Prat [14,15] and Laurindo and Prat [16,17] studied pattern formation during drying assuming capillary forces only and ignoring viscous forces. The importance of film flows was also discussed [17]. Based on the assumption of percolation patterns and under isothermal conditions, they proceeded to compute evaporation and drying rates by solving a quasi-static diffusion equation in the gas phase. However, earlier drying experiments in glass-bead packs by Shaw [11] suggested that viscous forces are not negligible, and in fact are needed to explain the formation of a front width (separating continuous liquid from gas) of a finite size. This, Shaw [11] attempted to scale using scaling expressions obtained from external drainage (see below). Despite the limitation on viscous forces, however, Prat’s studies are important in that

they represent the first attempt to theoretically characterize drying patterns and their rate of change in porous media.

As in other processes involving two-phase, immiscible flows in porous media, the following two aspects of drying patterns need to be understood: (i) Their geometrical structure, which dictates transport and capacitance and (ii) their rates of change. This is the main motivation of this paper. We consider the application of a pore-network approach, as in Nowicki, Davis, and Scriven [13], Prat [14,15], and Laurindo and Prat [16], but with specific objectives to understand the structure of drying patterns, particularly in the frontal region. From such an analysis, the derivation of effective macroscopic models can then be obtained. Drying, involving gas-liquid interfaces, can benefit from advances in the analogous problem of external drainage, which is reviewed below. What is novel in drying, however, is the additional effect of mass transfer in the gas phase, which actually drives the process. This needs to be analyzed in some detail.

The paper is organized as follows: First, we give a brief review of recent findings in isothermal drainage processes, which have a direct bearing on drying. Then, experiments in 2D micromodel geometries are presented to visualize mechanisms during drying and to help in the development of the theory. Based on the experimental observations, a theoretical approach is subsequently developed, which combines arguments borrowed from isothermal drainage and from the related bubble growth problem, where mass transfer is a key process. We use scaling arguments to show that drying is actually a process of invasion percolation in a stabilizing gradient (IPSG) (see below for a definition), from which we can infer the scaling of the front width as a function of the drying parameters. To demonstrate the transition from a percolation-only pattern, which was studied by Prat, to a stabilizing gradient and an IPSG, a linear stability analysis of the front in the appropriate geometries must be performed. This analysis will precede the main theoretical developments. We close by providing a framework for a macroscopic description based on transverse averages, and by commenting on the modeling of the other regimes.

We show that the scaling so obtained is compatible with Shaw’s [11] experimental results. Thus, although near the leading edge of the front, the displacement pattern will be of the percolation type (assumed by Prat and co-workers to be valid for the entire pattern), as the width of the front increases, viscous forces become increasingly important, leading to a displacement described by IPSG. Our analysis also sheds light to a process of liquid flow, termed “capillary pumping” by Le Romancer *et al.* [6], in their modeling of oil recovery from fractured reservoirs by gas injection. We show that this effect is actually the consequence of accounting for both capillary and viscous terms in the process. As in previous pore-scale studies in drying (Nowicki, Davis, and Scriven [13], Prat [15]), our analysis is restricted to isothermal problems. We also neglect convection in the gas phase, which is expected to be progressively of secondary importance, and gravity. The effect of the latter can be directly incorporated. However, effects of heat transfer and convection need a separate analysis, which will be attempted in a future study.

## II. PRELIMINARIES

Drying involves gas-liquid interfaces and mass transfer and should be subject to an analysis similar to external drainage and to bubble growth in porous media. Because of the expected similarities, we briefly review in this section recent advances in these two areas.

Consider first, drainage, namely, the displacement of a wetting phase by a nonwetting phase in a porous medium in the absence of phase change. In drainage, menisci reside in pores or at the entrance of pore throats with a curvature corresponding to the local capillary pressure, defined as the difference between the nonwetting (gas) and wetting (liquid) phase pressures,

$$P_c \equiv P_{nw} - P_w = 2\gamma\mathcal{H}. \quad (1)$$

Here,  $\gamma$  is the interfacial tension between the fluids,  $\mathcal{H}$  is the mean curvature of the meniscus and a zero contact angle was assumed. In the absence of buoyancy and/or viscous forces, the capillary pressure, thus the mean curvature, is spatially uniform. A meniscus will penetrate a pore throat, adjacent to which it resides, when the capillary pressure first exceeds the capillary entry pressure for that pore throat (roughly equal to  $2\gamma/r$ , where  $r$  is the pore throat size). In drainage at constant rate, the sequence of pore penetration can be modeled by invasion percolation (IP), where at each time step only one pore throat is invaded, that with the least capillary resistance (or, equivalently, the largest radius) among all throats at the perimeter of the interface. During this step, all other menisci remain stationary or fluctuate slightly. This type of displacement gives rise to a self-similar fractal pattern in the displacing phase, which eventually approaches that of the percolation cluster. The properties of the latter have been discussed in detail in various publications [19,20]. Because of the self-similarity involved, however, defining a mean-front position is not operationally useful.

However, if gravity and/or viscous forces are also important, a percolation pattern will not develop over the entire region of displacement. When only gravity forces are important, the capillary pressure will vary with the elevation  $h$  of the interface, since  $P_c = g_x \Delta\rho h$ , where  $g_x$  is the component of gravity in the direction of displacement and  $\Delta\rho = \rho_w - \rho_{nw}$ . Then, the displacement acquires the features of a different pattern, namely, invasion percolation in a gradient (IPG) [21–26]. In this case, the competition between gravity and capillary forces is expressed through the Bond number,

$$B = \frac{g_x \Delta\rho k}{\gamma}, \quad (2)$$

where  $k$  is the permeability of the porous medium (which is roughly proportional to the square of a mean pore size  $k \sim r_m^2$ , Katz and Thompson, [27]). Now, one needs to further distinguish two cases:

(i) If  $B > 0$ , for example, in the downwards displacement of a heavier by a lighter fluid, the two phases are separated by a front of finite width  $\sigma_G$ , which scales with the Bond number as [21,22]

$$\sigma_G \sim B^{-\nu/(\nu+1)}, \quad (3)$$

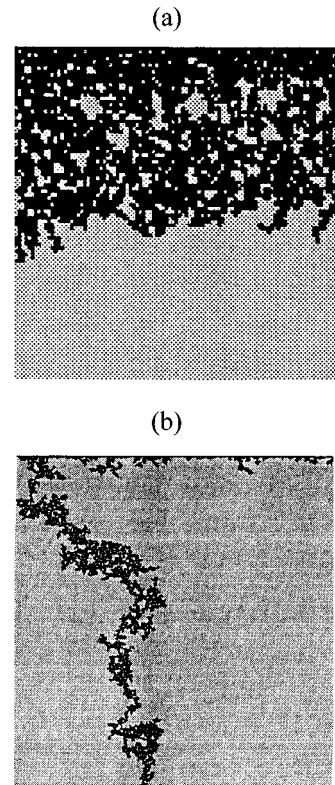


FIG. 3. (a) Self-affine front during external drainage indicating an IPSG process. (From Xu, Yortsos, and Salin [33].) (b) Single finger in external drainage indicating an IPDG process. (From Chaouche *et al.* [26].)

where  $\nu$  is the correlation length exponent of percolation. For a nonzero  $B$ , the front width is finite. Then, the front is not self-similar, but rather self-affine [28] [Fig. 3(a)]. Within the front, the pattern has the fractal characteristics of the percolation cluster. However, upstream of the front, the pattern is compact. Thus, a mean front position can be usefully defined. In essence, this reflects the transition of the displacement from an IP to a pistonlike pattern. The latter is the pattern that develops when only gravity (and not capillarity) acts (and which would be pistonlike in this case). We shall refer to this as IPSG. Hulin *et al.* [23] experimentally demonstrated the application of IPG in a drainage problem stabilized by gravity.

(ii) On the other hand, if  $B < 0$ , for example, in the downwards displacement of a lighter by a heavier fluid, the displacement is invasion percolation in a destabilizing gradient (IPDG). This pattern has the different features of capillary fingering [Fig. 3(b)], in which the displacement occurs by invading fingers of a mean width still given by Eq. (3), the local characteristics of which are still controlled by percolation. This regime has been discussed in detail in Frette *et al.* [29] and Meakin *et al.* [30].

The effect of viscous forces is more complex. At larger scales, where viscous effects predominate, two limiting patterns are expected, pistonlike displacement (PD) and viscous fingering, depending on whether the ratio  $M = \mu_w / \mu_{nw}$ , between the viscosities of the two fluids, is smaller or greater than 1, respectively. Essentially, this reflects the Saffman-Taylor instability [31]. At smaller scales, however, where capillary forces are important, the problem becomes similar

to IPDG (case of small  $M$ ) or IPDG (case of large  $M$ ) (Yortsos, Xu, and Salin [32], Xu, Yortsos, and Salin [33]). In the first case, in particular, fully developed drainage involves an advancing front of a finite width  $\sigma_V$ , as in the case of stabilizing gravity, followed by a more compact pattern. The front width can be shown to scale with the front capillary number,  $Ca_F = v\mu_{nw}/\gamma$ , as [34,33]

$$\sigma_V \sim \left( \frac{Ca_F}{\Sigma} \right)^{-\nu[1+\zeta+\nu(D-1)]}, \quad (4)$$

where  $v$  is the front velocity,  $\mu$  denotes viscosity,  $\Sigma$  is the dimensionless variance of the pore-size distribution,  $\zeta$  is the conductance exponent of percolation, and  $D$  is the fractal dimension of the percolation cluster. Values for the various percolation exponents can be found in classical texts on percolation, for example, in Stauffer and Aharony [35]. The properties of these patterns and the conditions delineating the various regimes were recently discussed in detail in Yortsos, Xu, and Salin [32] and Xu, Yortsos, and Salin [33].

Although subject to similar considerations, drying also involves the additional effect of mass transfer in the gas phase, which actually drives the process. A certain analogy can be drawn between drying and the problem of bubble growth in porous media, recently investigated by Li and Yortsos [36,37], and Satik and Yortsos [38], where the driving force for phase change and the ensuing growth of the gas phase is diffusion of mass or heat in the liquid (for the case of solution gas or boiling, respectively). When a bubble (more properly a gas ‘‘cluster’’) grows in a porous medium, its pattern at small bubble sizes will be of the percolation type. However, at larger sizes, capillary forces are less significant, and the displacement pattern is controlled by diffusion and viscous (and gravity) effects (Satik, Li, and Yortsos [39]). Diffusion in the liquid is known to destabilize such a liquid-to-gas phase change, leading to a Mullins-Sekerka instability (see [40,41] for the particular application), thus the pattern gradually becomes of the viscous fingering type. The boundaries in the parameter space that delineate patterns in bubble growth were described in Satik, Li, and Yortsos [39] by using scaling arguments and pore-network simulations. The same authors also proposed kinetic expressions to describe the rates of growth of bubble-growth patterns. Key to their description was the modeling of the diffusion process and its coupling with viscous and capillary phenomena. Such an approach could also be fruitfully used in the context of drying.

It could be noted that because it is essentially a process of gas displacing liquid, one might naively anticipate drying to involve IPDG patterns of the viscous fingering type, in analogy with external drainage in which the displacing fluid is less viscous, or with the bubble-growth problem at large sizes. However, this is misleading: drying is not driven by external injection, but by *internal* diffusion in the gas phase. This differs from external drainage, but also from bubble growth, where diffusion occurs in the liquid phase. These processes conspire to give patterns that are characterized by the stabilizing IPDG process, as will be shown below.

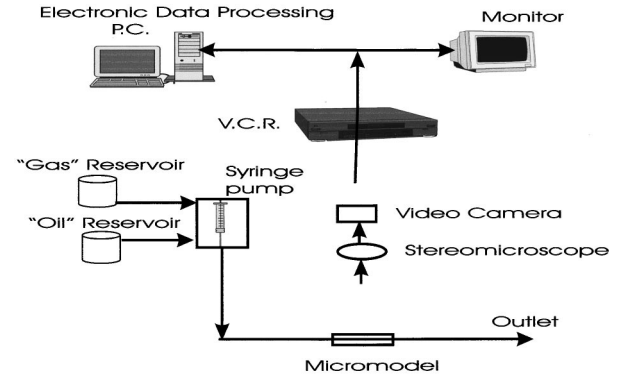


FIG. 4. Schematic of the experimental apparatus.

### III. EXPERIMENT

To visualize the mechanisms involved in drying in porous media we conducted experiments in transparent etched-glass micromodels. These micromodels consist of two glass plates fused together, on one of which a specific square pore network pattern is etched. Micromodels have been valuable in providing an understanding of the qualitative features of various displacement processes in porous media (see Buckley [42] for a review). In the context of phase change, a most recent application involves the bubble-growth experiments reported in Li and Yortsos [36] and the drying experiments by Laurindo and Prat [16]. In our application, the typical micromodel has size  $25\text{ cm} \times 10\text{ cm}$ , while the etched pores are channels with an estimated depth of  $100\ \mu\text{m}$ . The pore body/throat thickness is spatially distributed, following a specified Rayleigh distribution, with an average pore throat radius of  $450\ \mu\text{m}$  and an average pore body radius of  $900\ \mu\text{m}$ . These dimensions are specified before etching the glass plate. Due to imperfections in the glass and the lack of precise control in etching and fusion, however, the final dimensions are somewhat different. Also, although originally rectangular, the channels can become ‘‘eye-shaped’’ after fusion, as pointed out by Chatzis, Morrow, and Lim [43] and Vizica and Payatakes [44]. The final shape depends on the time of fusion among other parameters. Details of the manufacturing procedure can be found in Chatzis [45]. One entry port and one exit port on opposite sides of the micromodel serve to inject and recover the fluids. The experimental apparatus shown in Fig. 4 consists of the micromodel, of two reservoirs for the supply of the liquid and gas phases (denoted in the figure as ‘‘oil’’ and ‘‘gas’’) of a syringe pump, a camera for visualization, a video tape recorder, and a data processing system. Typical liquids used were *n*-pentane, *n*-hexane, and distilled water. The gas phase in the experiments was air.

The experiments consist of first saturating the micromodel with the liquid phase and subsequently displacing it with the gas at relatively high injection rates until the liquid phase is macroscopically disconnected from the two ports. At that time the gas injection rate was decreased to low rates and the drying process commences. This arrangement is actually different on the macroscopic scale than Shaw’s [11], where only one side is open to flow, there is no primary drainage or external liquid displacement, and the only mechanism for the movement of menisci is due to mass transfer. However, the basic drying mechanisms at the microscale are the same in

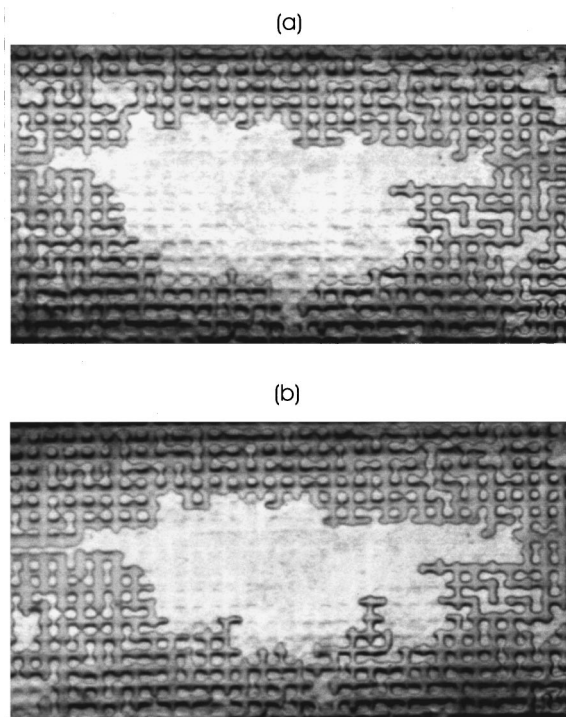


FIG. 5. Two different snapshots [(a) and (b)] of the interfacial patterns at two different times from the micromodel experiments (system: air/*n*-hexane). The linear dimensions are 6.5 cm  $\times$  3.5 cm.

both experiments. In fact, the theoretical model to be developed below will pertain to Shaw's configuration. The main difference is in mass transfer, which in our experiments can also occur by forced convection due to the particular configuration (see also Jia, Shing, and Yortsos [46] for a related application). In most of the experiments, however, the injection rate was kept quite low (of the order of 0.052 ml/min) resulting into small Peclet numbers and a predominantly diffusive mass transfer mechanism.

Figure 5 shows two snapshots of the interfacial pattern at different times during drying. The evaporation of the liquid and the resulting receding of the interface at various places are apparent. We note the existence of many clusters of different sizes, containing macroscopically disconnected liquid. The clusters are disordered and reflect the difference in the capillary characteristics of different pores. The interface is generally "rough," although it is difficult to ascertain self-affinity or self-similarity. Important findings from the visualization experiments included the following:

(i) Typically, the penetration of gas into the liquid and the receding of the meniscus occurred in the form of sudden jumps, one at a time, which were separated by finite time intervals. These jumps known as "rheon" events in external drainage, reflect the fact that for a pore to be invaded, a capillary pressure threshold must be exceeded, following which displacement and filling of the adjacent pore body will occur rapidly. During that time, interfaces pinned by capillarity in other pores are adjusted as a result of liquid incompressibility (see also below). Rheon events will predominate when the displacement is controlled by capillarity, as was the case in many of these experiments. When, however, drying rates are fast, as was the case with the experiments involving *n*-pentane, or at higher gas injection rates, the displacement

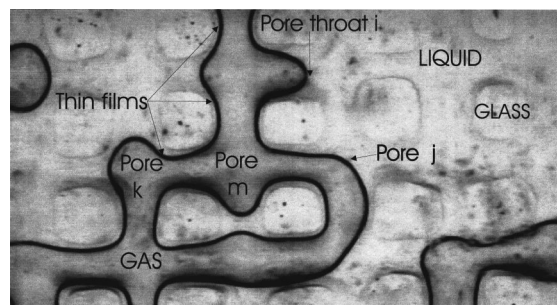


FIG. 6. Close-up of the gas-liquid interface during drying in the micromodel experiments. The linear dimensions are 1.0 cm  $\times$  0.5 cm.

was also found to occur at the same time in more than one pores, although several interfaces remained pinned during the same time.

(ii) Even though the plan views in Fig. 5 indicate gas-only occupied regions, a careful monitoring of the changes in the liquid-gas interface revealed that liquid films existed at the surfaces of pores invaded by gas. Figure 6 is a close-up of the gas-liquid interface, and shows the trace of wetting films left behind during the invasion of a pore by gas. The existence of films was also indirectly deduced from observing the emptying of some pores occupied by liquid, which would be topologically impossible in the absence of connected films. Wetting films in corners and crevices following drainage of a wetting liquid have been documented in various drainage studies (e.g., see Lenormand, Zarcone, and Sarr [47]). In his experiments, Shaw [11] inferred that connected liquid films help in the transport of liquid towards the open edge of the cell where it can evaporate. Prat [14,15] and Laurindo and Prat [16,17] also reported the existence of thin liquid films.

The above mechanisms of the drying process will be incorporated in the pore-network theory to be developed subsequently. Before we proceed, however, it is necessary to understand large-scale effects of diffusion and mass transfer. These can be studied in the absence of capillarity and pore microstructure.

#### IV. FRONT STABILITY IN THE ABSENCE OF CAPILLARITY

It was pointed out in a previous section that while small-scale features of a displacement process are set by capillarity, larger-scale characteristics are set by transport (such as viscous flow or diffusion). This is certainly the case both in external drainage (Xu, Yortsos, and Salin [33]) and in bubble growth (Satik, Li, and Yortsos [39]). The percolation pattern will ultimately (at large capillary numbers, see also below) evolve into a pattern dictated by the large scale. To understand this pattern, and thus to infer whether the process will be of the IPSG or the IPDG type, the stability of drying in an effective porous medium in the absence of capillarity must be analyzed.

Consider a planar drying front advancing in an isotropic and homogeneous effective medium, with a geometry that mimics the experiments by Shaw [11], as shown in Fig. 7. The liquid phase consists of a vaporizing single component, while the gas phase is a mixture of two components at con-

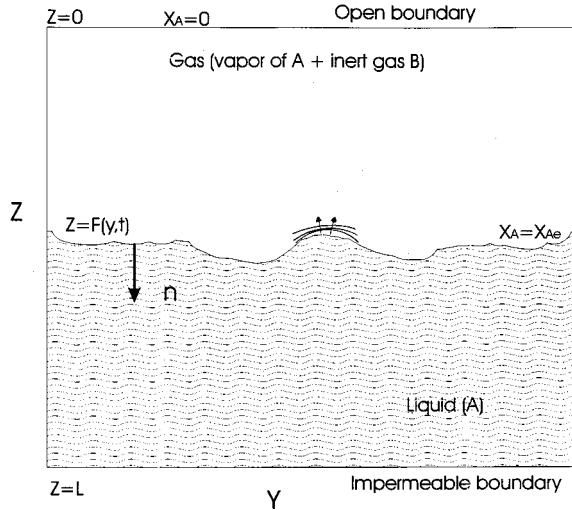


FIG. 7. A schematic of the planar drying front geometries for the stability analysis of drying in an effective porous medium. Near the indicated protuberance, concentration contours in the gas phase are compressed leading to enhanced mass transfer, hence to stabilization of the protuberance.

stant pressure. A sharp interface separates gas from liquid; thus, for the purposes of this section, we ignore effects of microstructure or film flows. Isothermal conditions are assumed. The top boundary is open to gas flow, has zero molar concentration of the vaporized liquid, and has a constant gas pressure. The bottom boundary is impermeable to liquid; thus all changes in liquid content are due to drying. We will examine the stability of the front to transverse perturbations in the absence of capillarity. For the purposes of this section, which is to reveal macroscopic features, the analysis will be based on a continuum description. We consider quasistatic diffusion in the gas phase and assume that the profiles (which are generally time-dependent) are “frozen” when the perturbation is imposed. Quasistatic diffusion is expected to be valid when the ratio of the equilibrium concentration of the volatile component in the gas phase to its molar density in the liquid phase is small, which is the case at low partial pressures (see Appendix). The more general problem involving unsteady-state diffusion and convection will be described in a separate study (see also Appendix). Assuming a frozen state during perturbations is a standard approach for the stability of time-varying base states (see, for example, Tan and Homsy [48]).

Let the front that separates liquid- from gas-occupied regions be denoted by the following equation in the notation of Fig. 7:

$$\mathcal{F}(z, y, t) \equiv z - F(y, t) = 0, \quad (5)$$

and recall the definitions

$$\mathbf{n} = \frac{\nabla \mathcal{F}}{|\nabla \mathcal{F}|} \quad (6)$$

and

$$v_n = - \frac{\mathcal{F}_t}{|\nabla \mathcal{F}|}, \quad (7)$$

for the outer normal (pointing towards the liquid) and the normal velocity at the front, respectively. The governing equations in the liquid-occupied region involve Darcy’s law for the flow of the liquid phase,

$$\mathbf{u}_l = - \frac{k}{\mu_l} \nabla P_l, \quad (8)$$

from which, and with the use of the continuity equation, we obtain a Laplace equation for the liquid pressure,

$$\nabla^2 P_l = 0. \quad (9)$$

This equation is subject to the following boundary conditions:

$$P_l = P_v \quad \text{at} \quad z = F(y, t), \quad (10)$$

where  $P_v$  is the gas pressure, assumed constant, due to the small gas viscosity, and

$$\frac{\partial P_l}{\partial z} = 0 \quad \text{at} \quad z = L, \quad (11)$$

where  $L$  denotes the longitudinal extent.

For negligible convection and transient effects the condensible component  $A$  satisfies the quasistatic diffusion equation (see Appendix),

$$\nabla^2 c_A = 0, \quad (12)$$

where  $c_A$  is the concentration of the condensible species (see also, Prat [14,15]). The corresponding boundary conditions are

$$c_A = 0 \quad \text{at} \quad z = 0 \quad (13)$$

and

$$c_A = c_e \equiv x_{Ae} c \quad \text{at} \quad z = F(y, t) \quad (14)$$

at the inlet and the front, respectively. Here, we defined the equilibrium mole fraction,  $x_{Ae} = P_{vA} / P_v$ , where  $P_{vA}$  is the partial pressure of  $A$ , and the total gas concentration  $c$  that because of the assumed constant pressure, can also be taken as a constant ( $c = P_v / RT$  for an ideal gas, where  $R$  is the ideal gas constant and  $T$  is the absolute temperature).

Concentration and pressure fields are coupled at the interface by mass balances. For the vaporizing liquid, we have

$$- \mathcal{D}_{AB} \frac{\partial c_A}{\partial n} = \frac{\rho_l}{M_A} (u_{ln} - v_n) \quad \text{at} \quad z = F(y, t), \quad (15)$$

where  $\mathcal{D}_{AB}$  is the diffusion coefficient,  $\rho_l$  is the mass density of the liquid,  $M_A$  is the molecular weight, and  $n$  denotes the normal to the interface. The interface is a material surface, thus,

$$v_n = u_{gn}. \quad (16)$$

The assumption made here is that the liquid consists of a single volatile component and that convection effects are secondary.

Consider, now, the base state in the absence of perturbations (denoted by superscript bar). Then, the front is located at  $z=f(t)$  and we readily find the base state.

$$\bar{c} = \frac{z c_e}{f(t)} \quad \text{for } 0 < z < f(t), \quad (17)$$

$$\bar{P}_l = P_v \quad \text{for } f(t) < z < L, \quad (18)$$

and

$$\bar{v}_n = \bar{v}_z \equiv \dot{f} = \frac{c_e M_A \mathcal{D}_{AB}}{\rho_l f}. \quad (19)$$

The latter can be integrated to yield the front location [assuming  $f(0)=0$ ],

$$f = \sqrt{(2c_e M_A \mathcal{D}_{AB} t / \rho_l)}. \quad (20)$$

This expression also results in the quasistatic limit from the more general analysis presented in the Appendix.

For the stability analysis we assume a ‘‘frozen’’ state at  $t=t_0$ , take normal modes, varying as  $\exp[i\alpha y + \omega(t-t_0)]$ , namely,

$$c = \bar{c} + \epsilon \sigma(z, t) \exp(i\alpha y + \omega t), \quad (21)$$

$$P_l = P_v + \epsilon \Pi(z, t) \exp(i\alpha y + \omega t), \quad (22)$$

and

$$F(y, t) = f(t) + \epsilon \exp(i\alpha y + \omega t), \quad (23)$$

and inquire about the sign of the rate of growth  $\omega$ , of disturbances of wave-number  $\alpha$ . In the above notation,  $\epsilon$  has dimensions of length. Substituting Eq. (21) to Eq. (12) and the boundary condition (13) gives

$$\sigma = 2A \sinh(\alpha z). \quad (24)$$

The constant  $A$  is evaluated by using boundary condition (14) and the base state solution evaluated at the front location. After some calculations we arrive at the result,

$$\sigma = - \frac{c_{Ae} \sinh(\alpha z)}{f \sinh(\alpha f)}. \quad (25)$$

Working likewise with the pressure field we find that  $\Pi$  satisfies a Laplace equation, the solution of which is subject to the no-flux and constant pressure conditions at the two boundaries, respectively, is identically zero,  $\Pi=0$ . Thus, at this level of approximation, the liquid phase is stagnant, as intuitively expected. However, consideration of capillarity at the microscale (and the interfacial curvature it implies) leads to viscous flow in the liquid phase, as will be shown below. This flow will set the main features of the drying pattern at the microscale.

A final substitution of the above into the coupling equation at the front leads to the following expression for the rate of growth of disturbances:

$$\omega = - \frac{\mathcal{D}_{AB} M_A c_{Xe} \alpha}{\rho_l f \tanh(\alpha f)} < 0. \quad (26)$$

It is apparent that the rate of growth  $\omega$  is negative, which implies that this displacement is unconditionally stable. The physical interpretation of the stability result is straightforward: If a protuberance of the front into the gas region forms, gas-phase diffusion rates will be higher at the tip compared to the base, due to the compression of isoconcentration curves at the tip (Fig. 7). In the absence of liquid flow, this will result in a locally larger velocity at the tip, hence in the smoothing of the protuberance, and in stability. Thus, even though it is effectively a process of a less viscous fluid displacing a more viscous fluid in a porous medium (where in external drainage one would expect a viscous fingering instability), the fact that the process is driven internally by diffusion in the gas phase renders the frontal displacement a stable process. In a sense, this is analogous to the melting of a solid, in which the receding interface is also linearly stable (Langer [40]). On the other hand, this is in contrast with the problem of bubble growth in porous media referred to above, where the process is also internally driven by diffusion, although in the liquid phase, and where in the absence of capillarity, the problem is linearly unstable (Li and Yortsos [41]). The phase change analogy with that problem is solidification in a supersaturated solution.

The important implication of the previous analysis is that in the absence of capillary forces the drying pattern in the porous medium will be PD. Because of the relatively low drying rates in applications, however, capillarity will be important over sufficiently small scales (compare with Fig. 5) and must be considered, as shown below. Before we proceed, we note that a qualitatively similar result to Eq. (26) is also expected in the more general problem, where net gas phase convection is considered. This analysis, which also includes spherical geometries, will be considered in a separate study.

## V. FRONT DESCRIPTION USING A PORE-NETWORK ANALYSIS

Consider now a description of the frontal region during drying by accounting for the effect of the pore structure (Figs. 5 and 6). Locally, the interface is described by an equation similar to Eq. (5), across which boundary conditions (15) and (16) apply. However, here menisci in the pore space must conform to the curvature of the pore in which they reside. Thus, across the meniscus, liquid and vapor pressures are related through the capillary pressure

$$P_l = P_v - \frac{2\gamma}{r}, \quad (27)$$

where, assuming locally spherical shapes, the mean pore radius of curvature is  $r$ . A convection-diffusion equation describes mass transfer in the vapor phase, while the fluid flow in both phases is described locally by Stoke’s law. In the following, we will focus on the structure of the front. For this, capillarity must be considered. We will show first that the latter induces a viscous flow, the magnitude of which dictates the extent of the front and its pattern. Then, the scaling of the front width and the basic properties of the pattern are discussed.

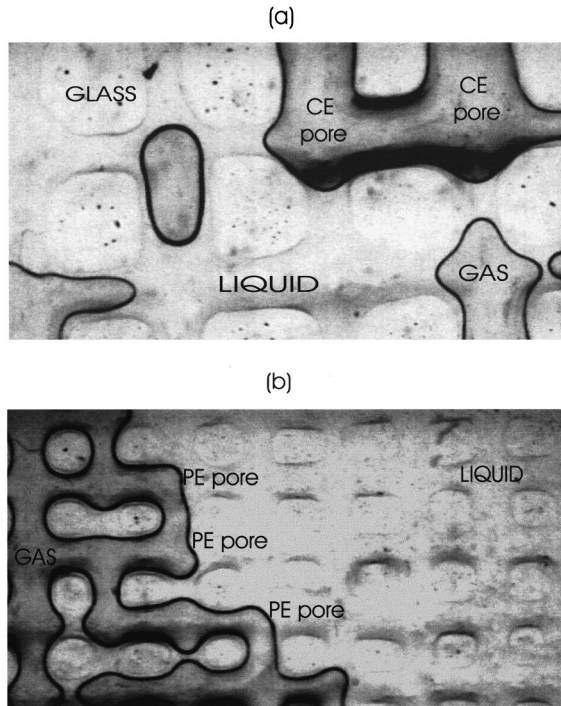


FIG. 8. Experimental visualization of two different types of pores during drying: (a) CE pores and (b) PE pores. The linear dimensions are (a) 0.6 cm  $\times$  0.4 cm and (b) 1.4 cm  $\times$  0.8 cm.

#### A. Capillarity-induced flow (capillary pumping)

Because of the capillary forces in the constriction of pore throats, a meniscus will not penetrate a pore throat, for example, throat  $i$  of radius  $r_{p,i}$  in Fig. 6, until the capillary pressure across the meniscus exceeds for the first time the capillary barrier of that throat,  $2\gamma/r_{p,i}$ . Until this happens, the normal velocity of this meniscus will be negligible; therefore, the meniscus will remain *pinned*. During this period of time, however, diffusion proceeds over the entire gas-liquid interface that requires that menisci will be receding in other pores of size greater than  $r_{p,i}$  (for example, pore  $j$  in Fig. 6) or along corners containing nondisplaced liquid. Thus, at any time during the process, the drying front will reside in pores of two different types: (i) completely empty (CE) [Fig. 8(a)], in which menisci are stationary at the pore throats and (ii) partly empty (PE) [Fig. 8(b)] in which menisci are receding. Partly empty pores are either pore bodies, or pores containing liquid left behind in corners, crevices, or films and which might be connected hydraulically to the bulk liquid. The rate of meniscus displacement due to evaporation is determined from the solution of the overall problem. When the capillary pressure barrier across a throat adjacent to a CE pore is exceeded, the corresponding pore is invaded and becomes a PE pore.

Consider now Eq. (15) applied to the meniscus on the CE pore throat  $i$ . Since evaporation continues occurring, regardless of whether the meniscus is stationary or moving, the normal liquid velocity  $u_{ln}$  in Eq. (15) must be negative. This implies a liquid flow in the direction from receding to stationary menisci (for example, from the PE pore containing capillary  $j$  to the CE pore containing capillary  $i$ ). It follows that capillary forces in a drying process will induce a flow, the magnitude of which depends on the drying rates. This is

to be contrasted to the prediction of a stagnant liquid obtained from the linearized stability analysis above, where capillarity was neglected. This flow is due to the variation of pore throat curvatures and it is capillarity driven (from “large” to “small” capillaries). In the particular application involving gas injection to recover oil from fractured rocks, a simplified process of the same type was termed *capillary pumping* by Le Romancer *et al.* [6].

#### B. Drying patterns

The capillarity-induced flow will impart a corresponding viscous pressure gradient; hence,

$$P_{l,j} > P_{l,i}. \quad (28)$$

Then, under the further assumption of a constant pressure in the gas,

$$P_{c,i} > P_{c,j}, \quad (29)$$

namely, as drying continues, the capillary pressure will be positive and may also increase with time in locations where the meniscus is stationary and pinned (CE pores of type  $i$ ). An analogous statement was also made by Shaw [11], although in his analysis it was attributed to countercurrent gas-liquid flow. It is possible, therefore, that after sufficient time has elapsed, the capillary barrier at such a pore throat  $i$  will be exceeded for the first time and the meniscus at that location will also start receding. This mechanism restricts the development of the front that cannot be extended too much, or become very tortuous, but will be limited instead to a finite width. To estimate its extent, we need to analyze the pattern developed.

Assume for a moment that the drying pattern of the front is of the IP type, as assumed, for example, by Prat [14,15]. Then, *all but one* of the pore bodies containing the front would be of the CE type, the only PE pore being that invaded from a pore throat with the least capillary barrier, among all throats currently containing front menisci. As shown above, however, there would be liquid flow from the PE pore to a CE pore, which may ultimately cause one or more pore throats to be invaded, even though their capillary barrier is not the smallest among the perimeter throats, as originally assumed. Under such conditions, therefore, the evolution of the IP pattern would be disrupted.

The analysis is facilitated if we make the following assumptions:

(a) The pressure drop across two adjacent pore bodies (e.g., sites  $k$  and  $m$  in Fig. 6) can be approximated by a Poiseuille-type law,

$$Q_{k \rightarrow m} = \frac{G_{km}}{\mu_l} (P_{l,k} - P_{l,m}), \quad (30)$$

where  $Q_{k \rightarrow m}$  is the flow rate across the two sites and the conductance  $G_{km}$  depends only on the geometry. This is a standard assumption in modeling displacements in porous media (e.g., see [13,36,37,49,50]).

(b) The pressure in the gas phase is spatially uniform. Given the small value of the gas viscosity compared to that of the liquid, this assumption is expected to be valid even at relatively large drying rates.

(c) The transport in the gas phase is by quasistatic diffusion only. Under certain conditions that favor large drying rates (for example, elevated temperatures), convection in the gas phase can be important. To infer its effect, however, the momentum balance in the gas phase needs to be considered. An extensive account of the more general problem using pore-network simulation will be considered in a separate study.

As inferred from the linearized stability analysis above, in the absence of capillarity, the front would be pistonlike, with some local roughness. Capillarity will keep interfaces, otherwise favored to grow by diffusion, pinned in place, until their capillary pressure barrier is exceeded. The characteristic length over which percolation rules apply and the pattern is of the IP type is estimated below.

Consider drying in a pore network of lateral extent  $L$ . We will denote the dimensionless mean position of the front by  $X_f(t)$  and its width by  $\sigma_{ft}(t)$ , or by  $\sigma_f(t)$ , where after sufficiently large time  $\sigma_{ft}(t)$  [or  $\sigma_f(t)$ ]  $\ll X_f(t)$ . Here, lengths have been dimensionalized using the pore length  $l$ , subscript  $ft$  indicates front tail in 3D and subscript  $f$  indicates front in 2D geometries (e.g., see Gouyet, Rosso, and Sapoval [24], for the difference in the two geometries). Contrary to the case of a 2D square lattice, to be discussed below, here both phases can be continuous simultaneously.

If we were to neglect any viscous pressure drop in the liquid phase, the capillary pressure, hence the percolation probability  $p$ , on the front would be spatially constant (the percolation probability being equal to the percolation threshold  $p = p_c$ , where, for 3D cubic lattices,  $p_c = 0.25$  and for 2D square lattices,  $p_c = 0.5$ ). Due to the capillary pumping mechanism described earlier, however, the capillary pressure, hence the percolation probability, will vary spatially. For a constant gas pressure, the characteristic variation  $|\Delta P_c|$  across the front is related to that of the liquid pressure, namely,

$$|\Delta P_c| = |\Delta P_l|. \quad (31)$$

Because the flow of the liquid in a pore network can be described by Poiseuille's law, and the displaced phase is continuous, then,

$$|\Delta P_l| \sim \frac{u_D \mu_l \sigma_{ft} l}{k}, \quad (32)$$

where we introduced the characteristic velocity  $u_D$  and the permeability  $k$  (which scales approximately as  $l^2$ ). The characteristic velocity  $u_D$  is due to diffusion, and to a first approximation,

$$u_D \sim \frac{\mathcal{D}_{AB} M_{AC}}{\rho_l} \left| \frac{\partial x_A}{\partial n} \right| \sim \frac{\mathcal{D}_{AB} M_{AC} x_{Ae}}{\rho_l l X_f}, \quad (33)$$

where we estimated concentration gradients in the gas phase by their base-state values. Substitution into Eq. (31) gives the following result for the variation of  $P_c$  in the front region;

$$|\Delta P_c| \sim \frac{\mathcal{D}_{AB} M_{AC} x_{Ae} \mu_l}{\rho_l l^2} \frac{\sigma_{ft}}{X_f}. \quad (34)$$

Equations (32)–(34) are order-of-magnitude estimates. Determining the exact pressure and concentration fields requires the solution of flow and transport problems in a disordered pore network, which are coupled at the front according to Eq. (15), with  $v_n = 0$  for all CE pores and with  $u_n = \sum_f u_n / N_f$ , for the single PE pore, where the sum is over all  $N_f$  CE pores at the front. The development of such a simulator is currently in progress [51]. Nonetheless, order of magnitude estimates are useful for obtaining scaling relations.

Consider now the variation of the percolation probability in the front region, which will be affected by the variation of  $P_c$ . The two are related as follows:

$$|\Delta P_c| \sim \frac{2 \gamma \Sigma}{r_m} |\Delta p|, \quad (35)$$

where  $\Sigma$  is the dimensionless variance of the pore size distribution  $\alpha(r)$ , and  $r_m$  is a characteristic pore size. In the derivation of Eq. (35) we made use of the results  $P_c = 2 \gamma / r$  and  $p = \int_r^\infty \alpha(r) dr$ . Use of Eq. (35) in Eq. (34) and substituting  $r_m \sim l$  gives the following expression for the variation of  $p$ :

$$|\Delta p| \sim \frac{C a_D}{2 \Sigma} \frac{\sigma_{ft}}{X_f}, \quad (36)$$

where we introduced a diffusion-based capillary number  $C a_D = \mathcal{D}_{AB} M_{AC} \mu_l x_{Ae} / \gamma l \rho_l$ . This capillary number includes the supersaturation  $C_e = c x_{Ae}$ , which drives the drying process, leading to the characteristic velocity  $\mathcal{D}_{AB} / l \sim \mathcal{D}_{AB} / \sqrt{k}$ . A similar diffusion-based capillary number was used in the related phase change problem involving bubble growth by Li and Yortsos [36,37], and Satik, Li, and Yortsos [39]. This reflects the fact that drying is internally driven and differentiates the process from external injection.

The final step for determining  $\sigma_{ft}$  makes use of a self-consistency argument, similar to IPG. As the process in the frontal region is in the percolation regime, then  $p$  must follow the percolation scaling [24],

$$|p - p_c| \sim \sigma_{ft}^{-(1/\nu)}. \quad (37)$$

Substitution of Eq. (37) in Eq. (36) gives the final scaling result,

$$\sigma_{ft} \sim \left( \frac{2 \Sigma X_f}{C a_D} \right)^{\nu/(1+\nu)}, \quad (38)$$

This equation sets the length scale at the front over which the IP pattern is valid. By definition, this length scale coincides with the front-tail width. The scaling is identical to that in IPG, provided that the Bond number is identified as  $B = C a_D / 2 \Sigma X_f$ . According to Eq. (38), the front width increases as the capillary number decreases, as the front position increases (namely, as the drying rates slow down), or as the disorder in the medium increases. Thus, wider fronts are expected for higher values in the interfacial tension, smaller

liquid viscosities, and larger drying times. Given that the velocity of the front  $v_f$  is inversely proportional to its mean position (recall the base-state scaling  $X_f \sim \sqrt{t}$ ), we further rewrite Eq. (38) as

$$\sigma_{ft} \sim \left( \frac{2\Sigma}{v_f C a_D} \right)^{\nu/(1+\nu)} \quad (39)$$

This expression will be used below for a comparison with the experimental data. Finally, it is worth noting that the exponent found is identical to Lenormand's [49] for the delineation of the percolation limit in the drainage of a viscous fluid, even though the two problems are actually quite different.

We summarize this section as follows: During drying the frontal region consists of a front of a finite width  $\sigma_{ft}$ . Within the front, the displacement has the fractal properties of an IP interface. Upstream of the front, however, the displacement is compact. Therefore, the process can be approximated as IPSG. Xu, Yortsos, and Salin [33] show how various properties of the front during displacement processes can be approximated by simple versions of IPSG. The scaling of the width of the front is given by Eq. (38); thus, the front width is predicted to increase with increasing distance from the boundary. As in other problems, where growth is controlled internally, namely, by diffusion within one of the two phases, the appropriate capillary number is based on the diffusive strength and the supersaturation applied. Typical values obtained fall within the range of external drainage in porous media.

## VI. COMPARISON WITH EXPERIMENTS

To check the validity of the theory we used the experimental results of Shaw [11]. These experiments were conducted in a Hele-Shaw cell of thickness 15–20  $\mu\text{m}$ , packed with glass beads of size 0.5  $\mu\text{m}$ . We estimate that the cell consisted of 30–40 bead layers, thus pertaining effectively to a 3D geometry. The experimental configuration is similar to that studied theoretically above, with one side of the model open to purge the drying liquid, while all other sides were impermeable to flow. For these experimental conditions we estimated that  $C a_D$  is of the order of  $10^{-8}$ . Figure 9 reprinted from Shaw [11] shows in logarithmic coordinates the scaling of the front width with the front velocity. The least-squares fit to the data gives a straight line with slope  $-0.48 \pm 0.1$ . Compared to the theoretical equation (39), which also predicts a straight line with slope  $-0.47$  for 3D and  $-0.57$  for 2D, the agreement is, at first glance, quite good. However, a more careful comparison shows that this cannot be considered conclusive. Given that the front width in Shaw's experiments is several times larger than the spacing of the cell, it is likely that the pattern development is quenched along the third dimension, and that the experiment is effectively in a 2D geometry. Under such conditions, the agreement is not as strong. Furthermore, the 3D scaling was developed for the front tail width  $\sigma_{ft}$ , where the pattern is fractal, which may not be the same quantity experimentally measured. Thus, even under the assumption of a 3D pattern, theoretical predictions and experimental results may actually pertain to two different quantities (different definitions of

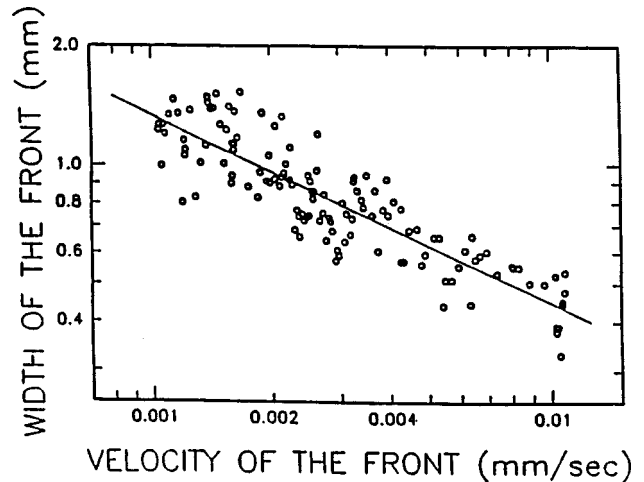


FIG. 9. Variation of the width of the drying front with its average velocity. A least-squares fit to the data gives an exponent of  $-0.48 \pm 0.1$ . (From Shaw [11].)

front width). For these reasons, although compatible with the experiments, the theory presented cannot be conclusively confirmed from these experiments.

Shaw [11] used Wilkinson's [34] theory for external drainage to interpret the experimental results. As discussed in a previous section, this power law has the dependence shown in Eq. (4) with an exponent that equals  $-0.38$  or  $-0.25$  in 2D or 3D, respectively. We believe, however, that the immiscible, external drainage theory is actually not relevant to the present problem that as explained above is driven by diffusion in the gas phase, and where the corresponding viscous pressure drop is in the displaced wetting phase. By contrast, scaling Eq. (4) reflects the stabilizing effect of viscous forces occurring in the *displacing* phase (which here is the relatively nonviscous gas phase, thus leading to an apparent contradiction) (see also Xu, Yortsos, and Salin [33]). The inadequacy of Eq. (4) was recognized by Shaw [11] who subsequently proposed a different power law similar to Eq. (39), without, however, elaborating on the mass transfer aspects of the problem.

## VII. IMPLICATIONS FOR A MACROSCOPIC DESCRIPTION

The previous section described the structure of the frontal region that because of its percolation and fractal characteristics requires a local analysis. In the upstream regimes, however, a macroscopic description is possible. The elements of this description are discussed below.

Consider first the pattern upstream of the front. The discussion will be restricted to 3D geometries, where flow in this regime is bicontinuous. Immediately adjacent to the front, there exists a bicontinuous region upstream of the leading edge, where the pattern is locally IP, except that now the process is above the percolation threshold, as an increasing number of smaller-size throats have been invaded. Assuming a sufficiently small slope in the liquid saturation profile, volume-averaged quantities can be defined; hence, we can postulate a continuous description in this region. The analogous problem for drainage processes was studied in Xu,

Yortsos, and Salin [33]. Using transverse averages, the mass balance on the liquid reads as

$$\rho_l \left[ \phi \frac{\partial S_l}{\partial t} + \frac{\partial q_{l,z}}{\partial z} \right] = -\mathcal{R}, \quad (40)$$

where the liquid flow rate  $q_{l,z}$  is expressed using a generalized Darcy's law,

$$q_{l,z} = - \frac{kk_{r,l}(S_l)}{\mu_l} \frac{\partial P_l}{\partial z}, \quad (41)$$

involving the relative permeability function  $k_{r,l}(S_l)$ . The liquid pressure is related to the capillary pressure function  $P_c(S_l)$  via

$$P_l = P_v - P_c(S_l). \quad (42)$$

The two functions  $k_{r,l}(S_l)$  and  $P_c(S_l)$  correspond to primary drainage, and they can be computed in a straightforward fashion using IP. The rate of evaporation,  $\mathcal{R} \equiv (\mathcal{D}_{AB} M_{Ac}/V) \int_{\mathcal{A}_{lg}} (\partial x_A / \partial n) dA$ , expresses the net mass transfer from the liquid to the gas phase, occurring over the gas-liquid interfacial area  $\mathcal{A}_{lg}$ , where  $V$  is volume and  $\mathbf{n}$  is the unit normal to the interface pointing towards the liquid. In the dilute-limit approximation considered here, this process is linear with respect to the concentrations; thus, we may further take

$$\mathcal{R} = \frac{\mathcal{D}_{AB} M_{Ac}}{l^2} (x_{Ae} - x_{Ag}) G(S_l), \quad (43)$$

where  $x_{Ag}$  is the transverse average of the mole fraction in the gas phase. Because the pattern of all interfaces is still dictated by IP (although here it is above the percolation threshold), the effective gas-liquid area and the dimensionless scaling function  $G(S_l)$  can be computed by solving a quasistatic diffusion problem around a percolation cluster. The results of this study will be reported elsewhere. We expect, however, that  $G$  has a nonmonotonic dependence, vanishing both near the front (where  $S_l \rightarrow 1$ ) and far upstream of the front (where  $S_l$  approaches zero).

The system of Eqs. (40)–(43) is completed with a mass balance for the volatile component in the gas phase. In the dilute limit, the overall mass balance reads

$$\phi \frac{\partial S_g}{\partial t} + \frac{\partial q_{g,z}}{\partial z} = 0, \quad (44)$$

while the mass balance for the volatile component becomes

$$\phi S_g \frac{\partial x_{Ag}}{\partial t} + q_{g,z} \frac{\partial x_{Ag}}{\partial z} = \frac{\partial}{\partial z} \left( \mathcal{D}(S_l) \frac{\partial x_{Ag}}{\partial z} \right) + \frac{\mathcal{R}}{c}, \quad (45)$$

where the diffusion coefficient  $\mathcal{D}(S_l)$  is to be computed from a percolation study. The system of Eqs. (40)–(45) can be solved to determine the saturation profiles in the regime of bicontinuous phases.

The regime far upstream of the front consists of disconnected ganglia of the liquid phase. Reasoning as in the scaling analysis for the front, we can conclude that their characteristic size has the same scaling as given for the front,

namely, Eq. (38), where now  $X_f$  denotes the average location of these stationary ganglia. The description of this problem can still be obtained with the above equations (40)–(45), except that the liquid velocity must now be set to zero. These problems are currently under study.

## VIII. CONCLUSIONS

In this paper we used concepts of immiscible displacements in porous media driven by mass transfer to model certain aspects of drying of porous media. Visualization experiments of drying in 2D glass micromodels were conducted to identify mechanisms concerning the motion of gas-liquid interfaces at the pore scale. Then, a pore network approach was introduced, utilizing arguments from isothermal drainage, particularly IPSG, and from the related bubble-growth problem.

A specific objective of this work was the analysis of the frontal region separating the initial liquid from the upstream two-phase region. A linear stability analysis in an effective porous medium, in the absence of capillarity or microstructure, showed that planar drying fronts are stable due to diffusion in the gas phase. For a porous medium with a microstructure, however, capillarity induces a viscous flow, termed in other contexts as ‘‘capillary pumping.’’ The developing pressure gradients effectively limit the extent of the front, which would otherwise be of the percolation type, to a finite width. In conjunction with the prediction of a macroscale stable front, capillarity, diffusion, and viscous effects result in a process similar to IPSG. A power-law scaling relation of the front width with a diffusion-based capillary number was then developed. This capillary number reflects the fact that the process is internally driven due to diffusion, as in bubble-growth problems but in contrast to external drainage. The scaling exponent predicted was found to be consistent with the experiments of Shaw [11], although a conclusive proof was not obtained. A continuum description was also developed for the regimes upstream of the front; the detailed analysis of which will be reported in a separate study.

## ACKNOWLEDGMENTS

The research of I.N.T. and Y.C.Y. was partially supported by U.S. DOE Contract No. DE-FG22-96BC1994/SUB. The research of S.P., A.K.S., and N.K. was partially funded by the JOULE Programme of the European Commission (Contract No. JOF3-CT95-0008). All of these sources of support are gratefully acknowledged. We would also like to acknowledge the help of N. Konstantinou and G. Petrou of NCRS ‘‘Demokritos’’ in the micromodel tests. I.N.T. would also like to acknowledge the hospitality of the Institute of Physical Chemistry of NCRS ‘‘Demokritos’’ where part of the experimental work was conducted.

## APPENDIX

In this appendix we consider the base state for the more general problem that includes unsteady-state diffusion and convection. The condensible component  $A$  satisfies the mass balance

$$\frac{\partial c_A}{\partial t} + \nabla \cdot \mathbf{N}_A = 0, \quad (\text{A1})$$

where  $\mathbf{N}_A$  is its molar flux, expressed for a binary mixture as

$$\mathbf{N}_A = -c\mathcal{D}_{AB}\nabla x_A + x_A(\mathbf{N}_A + \mathbf{N}_B). \quad (\text{A2})$$

Here,  $c_A$  is the molar concentration,  $x_A$  is the molar fraction of A ( $c_A = cx_A$ ), and  $\mathbf{N}_B$  is the molar flux of the noncondensable species. The latter is also conserved,

$$\frac{\partial c_B}{\partial t} + \nabla \cdot \mathbf{N}_B = 0. \quad (\text{A3})$$

The corresponding boundary conditions read

$$x_A = 0 \quad \text{at} \quad z = 0 \quad (\text{A4})$$

and

$$x_A \equiv x_{Ae} = \frac{P_{vA}(T)}{P_v} \quad \text{at} \quad z = F(y, t) \quad (\text{A5})$$

at the inlet and the front, respectively. The equilibrium vapor pressure  $P_{vA}$  is a function of temperature, among other factors.

For a porous medium, the mass-averaged velocity in the gas phase,  $\mathbf{u}_v = (M_A\mathbf{N}_A + M_B\mathbf{N}_B) / (\rho_A + \rho_B)$ , satisfies Darcy's law

$$\mathbf{u}_v = -\frac{k}{\mu_v} \nabla P_v, \quad (\text{A6})$$

where  $M$  denotes molecular weight. Because of the small gas viscosity, however, the gas pressure can be assumed constant, which for isothermal conditions also implies a constant molar concentration  $c$ . Note also, that from Eq. (A6) and the definition of the mass-averaged velocity, we have the general relation

$$\nabla \times \mathbf{u}_v = \mathbf{0}. \quad (\text{A7})$$

This can be used in the more general case where 2D concentration and pressure fields must be evaluated. Concentration and pressure fields are coupled at the interface by mass balances. For the vaporizing liquid,

$$j_{An} \equiv M_A N_{An} - \rho_{Ae} v_n = \rho_l (u_{ln} - v_n) \quad \text{at} \quad z = F(y, t), \quad (\text{A8})$$

while for the noncondensable component B,

$$j_{Bn} \equiv M_B N_{Bn} - \rho_{Be} v_n = 0 \quad \text{at} \quad z = F(y, t), \quad (\text{A9})$$

where  $\mathbf{j}$  is the mass flux,  $v_n$  is the velocity of the receding interface,  $\rho_l$  is the mass density of the liquid, and  $\rho_{Ae}$  and  $\rho_{Be}$  denote mass density of species A or B in the gas phase at equilibrium; thus  $\rho_{Ae} = x_{Ae} c M_A$ .

Consider now the base state in the absence of perturbations (denoted by superscript bar). Then, all fluxes are along the  $z$  direction only, the front is located at  $z = f(t)$  and the base state is described as follows. The base-state liquid pressure corresponds to a stagnant liquid,

$$\bar{P}_l = P_v \quad \text{for} \quad f(t) < z < L. \quad (\text{A10})$$

The base-state fluxes are

$$\bar{N}_{Az} \approx -\frac{\rho_l}{M_A} v_z \quad \text{and} \quad \bar{N}_{Bz} = \frac{\rho_{Be}}{M_B} v_z, \quad (\text{A11})$$

where we implied  $\rho_{Ae} \ll \rho_l$ , while the mole fraction is given from

$$\bar{N}_{Az} = -c\mathcal{D}_{AB} \frac{d\bar{x}_A}{dz} + \bar{x}_A(\bar{N}_{Az} + \bar{N}_{Bz}). \quad (\text{A12})$$

To solve the unsteady-state problem we take the *ansatz* that the front position is proportional to the square root of time,

$$f(t) = 2\lambda \sqrt{\mathcal{D}_{AB} t}, \quad (\text{A13})$$

where  $\lambda$  is a dimensionless parameter to be determined. Noting that for constant  $c$ , the total molar flux is constant,

$$N_{Az} + N_{Bz} = \rho_l \dot{f} \left[ \frac{\rho_{Be}}{\rho_l M_B} - \frac{1}{M_A} \right], \quad (\text{A14})$$

the mass balance for species A, Eq. (A1) reads

$$c \frac{\partial x_A}{\partial t} + \rho_l \dot{f} \left[ \frac{\rho_{Be}}{\rho_l M_B} - \frac{1}{M_A} \right] \frac{\partial x_A}{\partial z} = c\mathcal{D}_{AB} \frac{\partial^2 x_A}{\partial z^2}, \quad (\text{A15})$$

where we made use of Eq. (A11), dot denotes derivative with respect to time and we evaluated  $v_z$  at  $z = f(t)$ . We will seek the solution of this problem using the similarity variable  $\eta = z/2\sqrt{\mathcal{D}_{AB} t}$ . Then, Eq. (A15) becomes

$$x'' + 2x'(\eta - \phi) = 0, \quad (\text{A16})$$

where primes denote derivative with respect to  $\eta$  and we defined

$$\phi = \lambda \frac{\rho_l}{c} \left[ \frac{\rho_{Be}}{\rho_l M_B} - \frac{1}{M_A} \right]. \quad (\text{A17})$$

This equation is to be solved subject to the boundary conditions

$$x_A = x_{Ae} \quad \text{at} \quad \eta = \lambda \quad (\text{A18})$$

and

$$x_A = 0 \quad \text{at} \quad \eta = 0. \quad (\text{A19})$$

Note that because the integration interval here is  $0 < z < f(t)$  and  $f(0) = 0$ , there is no need to satisfy an initial condition, in contrast to the problems considered by Bird, Stewart, and Lightfoot [52] and Cussler [53]. The latter authors solved a similar problem, except that they made the assumptions of a fixed interface [52] or of a vanishing flux for species B [53].

The solution of Eqs. (A16)–(A19) is

$$x_A = x_{Ae} \frac{\text{erf}(\eta - \phi) + \text{erf} \phi}{\text{erf}(\lambda - \phi) + \text{erf} \phi}. \quad (\text{A20})$$

The unknown parameter  $\lambda$  is obtained by substitution of this solution in the first equation of (A11). After some manipulations, we find that  $\lambda$  solves the transcendental equation,

$$\lambda(1-x_{Ae}) = \frac{cx_{Ae}M_A \exp[-(\lambda-\phi)^2]}{\sqrt{\pi\rho_l}[\operatorname{erf}(\lambda-\phi) + \operatorname{erf}\phi]} \quad (\text{A21})$$

In Eq. (A21), it must be recalled that  $\phi$  is proportional to  $\lambda$  [see Eq. (A17)], and we assumed that the gas density is much smaller than the liquid density. Equation (A21) shows that the front grows proportionally to the square root of time, as expected. Of interest is the dilute limit  $[x_{Ae}[(M_A/M_B) \times (\rho_{Be}/\rho_l) - 1]] \ll 1$ , considered in the main text, in which case  $\lambda \ll 1$  and Eq. (A21) gives

$$\lambda^2 = \frac{x_{Ae}cM_A}{2\rho_l}, \quad (\text{A22})$$

which when inserted in Eq. (A13) gives

$$f = \sqrt{(2c\mathcal{D}_{AB}M_Ax_{Ae}/\rho_l)t}, \quad (\text{A23})$$

which is the equation in the text. In this limit, the convective term vanishes and the concentration field is quasistatic (namely, it satisfies a Laplace equation, the base-state profile for the mole fraction being linear).

- 
- [1] P. Chen and D. C. T. Pei, *Int. J. Heat Mass Transf.* **32**, 297 (1989).
- [2] W. T. Simpson, *Drying Technology* **2**, 235 (1983).
- [3] W. T. Simpson, *Drying Technology* **3**, 353 (1984).
- [4] M. Fortes and M. R. Okos, *Advances in Drying* (Hemisphere Publishing, New York, 1980), Vol. 1, pp. 119–154.
- [5] C. K. Ho and K. S. Udell, *Int. J. Heat Mass Transf.* **38**, 339 (1995).
- [6] J. F. Le Romancer, D. Defives, F. Kalaydjian, and G. Fernandes (unpublished).
- [7] Y. Le Gallo, J. F. Le Romancer, B. Bourbiaux, and G. Fernandes, Report No. SPE 38924 (unpublished).
- [8] K. M. Waananen, J. B. Litchfield, and M. R. Okos, *Drying Technology* **11**, 1 (1993).
- [9] M. Prat, *Drying Technology* **9**, 1181 (1991).
- [10] A. V. Luikov, *Heat and Mass Transfer in Capillary Porous Bodies* (Pergamon, London, 1966).
- [11] T. M. Shaw, *Phys. Rev. Lett.* **59**, 1671 (1987).
- [12] S. Whitaker, *Adv. Heat Transfer* **13**, 119 (1977).
- [13] S. C. Nowicki, H. T. Davis, and L. E. Scriven, *Drying Technology* **10**, 925 (1992).
- [14] M. Prat, *Int. J. Multiphase Flow* **19**, 691 (1993).
- [15] M. Prat, *Int. J. Multiphase Flow* **21**, 875 (1995).
- [16] J. M. Laurindo and M. Prat, *Chem. Eng. Sci.* **51**, 5171 (1996).
- [17] J. M. Laurindo and M. Prat, *Chem. Eng. Sci.* **53**, 2257 (1998).
- [18] V. Pot, C. Appert, A. Melayah, D. H. Rothman, and S. Zaleski, *J. Phys. II* **6**, 1517 (1996).
- [19] D. Wilkinson and J. F. Willemsen, *J. Phys. A* **16**, 3365 (1983).
- [20] J. Feder, *Fractals* (Plenum, New York, 1988).
- [21] D. Wilkinson, *Phys. Rev. A* **30**, 520 (1984).
- [22] B. Sapoval, M. Rosso, and J. F. Gouyet, *J. Phys. (France) Lett.* **46**, L149 (1985).
- [23] J. P. Hulin, E. Clement, C. Baudet, J. F. Gouyet, and M. Rosso, *Phys. Rev. Lett.* **61**, 333 (1988).
- [24] J. F. Gouyet, M. Rosso, and B. Sapoval, *Phys. Rev. B* **37**, 1832 (1988).
- [25] A. Birovljev, L. Furuberg, J. Feder, T. Jossang, K. J. Maloy, and A. Aharony, *Phys. Rev. Lett.* **67**, 584 (1991).
- [26] M. Chaouche, N. Rakotomalala, D. Salin, B. Xu, and Y. C. Yortsos, *Phys. Rev. E* **49**, 4133 (1994).
- [27] A. J. Katz and A. H. Thompson, *Phys. Rev. B* **34**, 8179 (1986).
- [28] A. L. Barabasi and H. F. Stanley, *Fractal Concepts in Surface Growth* (Cambridge University Press, Cambridge, 1995).
- [29] V. Frette, J. Feder, T. Jossang, and P. Meakin, *Phys. Rev. Lett.* **68**, 3164 (1992).
- [30] P. Meakin, J. Feder, V. Frette, and T. Jossang, *Phys. Rev. A* **46**, 3357 (1992).
- [31] P. G. Saffman and G. I. Taylor, *Proc. R. Soc. London, Ser. A* **245**, 312 (1958).
- [32] Y. C. Yortsos, B. Xu, and D. Salin, *Phys. Rev. Lett.* **79**, 4581 (1997).
- [33] B. Xu, Y. C. Yortsos, and D. Salin, *Phys. Rev. E* **57**, 739 (1998).
- [34] D. Wilkinson, *Phys. Rev. A* **34**, 1380 (1986).
- [35] D. Stauffer and A. Aharony, *Introduction to Percolation Theory* (Taylor & Francis, London, 1992).
- [36] X. Li and Y. C. Yortsos, *AIChE J.* **41**, 214 (1995).
- [37] X. Li and Y. C. Yortsos, *Chem. Eng. Sci.* **50**, 1247 (1995).
- [38] C. Satik and Y. C. Yortsos, *J. Heat Transfer* **118**, 455 (1996).
- [39] C. Satik, X. Li, and Y. C. Yortsos, *Phys. Rev. E* **51**, 3286 (1995).
- [40] J. S. Langer, *Rev. Mod. Phys.* **52**, 1 (1980).
- [41] X. Li and Y. C. Yortsos, *Phys. Fluids* **6**, 1663 (1994).
- [42] J. S. Buckley, in *Interfacial Phenomena in Petroleum Recovery*, edited by N. R. Morrow (Dekker, New York, 1990).
- [43] I. Chatzis, N. R. Morrow, and H. T. Lim, *SPE J.* **23**, 311 (1983).
- [44] O. Vizica and A. Payatakes, *PCH PhysicoChem. Hydrodyn.* **11**, 187 (1989).
- [45] I. Chatzis, New Mexico Institute of Technology, PRRC Report No 80-12, 1982 (unpublished).
- [46] C. Jia, K. Shing and Y. C. Yortsos, *J. Contam Hydrol.* **35**, 363 (1999).
- [47] R. Lenormand, C. Zarcone, and A. Sarr, *J. Fluid Mech.* **135**, 337 (1983).
- [48] C. T. Tan and G. M. Homsy, *Phys. Fluids* **29**, 3549 (1986).
- [49] R. Lenormand, *Proc. R. Soc. London, Ser. A* **423**, 159 (1989).
- [50] M. Blunt and P. King, *Transp. Porous Media* **6**, 407 (1991).
- [51] S. Poulou, A. K. Stubos, and Y. C. Yortsos (unpublished).
- [52] R. B. Bird, W. E. Stewart, and E. L. Lightfoot, *Transport Phenomena* (Wiley, New York, 1960).
- [53] E. L. Cussler, *Diffusion: Mass Transfer in Fluid Systems* (Cambridge University Press, Cambridge, 1984).